

Stability and Convergence of Nuclear Detonations in White Dwarf Collisions

PETER ANNINOS,¹ DAVID CRUZ-LOPEZ,² BRIGHTEN JIANG,³ AND EMANUEL GORDIS⁴

¹*Lawrence Livermore National Laboratory, Livermore, CA 94550, USA*

²*Department of Astronomy, University of Illinois, Urbana, IL 61801, USA*

³*Department of Astronomy, University of Florida, Gainesville, FL 32611, USA*

⁴*Department of Physics, Cornell University, Ithaca, NY 14853, USA*

ABSTRACT

We investigate the numerical stability of thermonuclear detonations in 1D accelerated reactive shocks and 2D binary collisions of equal mass, magnetized and unmagnetized white dwarf stars. To achieve high resolution at initiation sites, we devised geometric gridding and mesh velocity strategies specially adapted to the unique requirements of head-on collisional geometries, scenarios in which one expects maximum production of iron-group products. We study effects of grid resolution and the limiting of temperature, energy generation, and reactants for different stellar masses, separations, magnetic fields, initial compositions, detonation mechanisms, and limiter parameters across a range of cell sizes from 1 to 100 km. Our results set bounds on the parameter space of limiter amplitudes for which both temperature and energy limiting procedures yield consistent and monotonically convergent solutions. Within these bounds we find grid resolutions of 5 km or better are necessary for uncertainties in total released energy and iron-group products to drop below 10%. Intermediate mass products (e.g., calcium) exhibit similar convergence trends but with somewhat greater uncertainty. These conclusions apply equally to pure C/O WDs, multi-species compositions (including helium shells), magnetized and unmagnetized cores, and either single or multiple detonation scenarios.

Keywords: supernovae — white dwarfs — hydrodynamics — nuclear reactions, nucleosynthesis

1. INTRODUCTION

Although there is no universally accepted consensus on the thermonuclear initiation mechanism in Type Ia supernovae, it is generally believed explosions result from the nuclear detonation of white dwarf (WD) stars, even if the mechanism itself is not fully understood. For the case of colliding WDs, however, initiation is well-known to be triggered by shocks. What perhaps remains uncertain in these scenarios is the degree to which spatial (and temporal) resolution affects ignition and burn product distributions, or even whether ignition is initiated promptly at first contact, potentially affecting luminosities and their similarity to Ia-like events. This is an especially important consideration for multi-dimensional simulations straining computational resources to simultaneously cover the small detonation scales together with global binary dynamics, separated easily by more than four orders of magnitude.

In a recent study, [Katz & Zingale \(2019\)](#) (henceforth referred to as KZ19) proposed a set of one-dimensional shock tube problems, replicating conditions from their multi-dimensional work on WD collisions, as a proxy test to assess convergent behavior. Based on results from that study, they caution resolutions finer than a kilometer may be required to achieve convergent and consistent results. [Kushnir & Katz \(2020\)](#) (KK20) however contradict this conclusion and instead claim convergence for the same test problems at coarser resolutions of a few kilometers. In our own proxy studies of tidal disruption events (TDEs) we found better than 10% convergence for some attributes (like nickel production) below 10 km resolution, but significantly greater uncertainty in many transient products even at resolutions as low as 1 km ([Anninos et al. 2022](#)).

Summarizing the literature survey by KZ19, we note most calculations of WD collisions were run at resolutions between 10-100 km with SPH codes ([Rosswog et al. 2009](#); [Raskin et al. 2010](#); [Lorén-Aguilar et al. 2010](#); [García-Senz et al. 2013](#)), and 50-500 km with grid-based codes ([Rosswog et al. 2009](#); [Hawley et al. 2012](#)) with notable exceptions for calculations performed in axisymmetry ([Kushnir et al. 2013](#); [Papish & Perets 2016](#)). All of these studies managed to convert large amounts of material to iron-group elements, but did not agree quantitatively on final outcomes. In some cases the consistency (or convergence) of behaviors with resolution was not discussed. In others claims were

made suggesting convergent behavior but either over a small dynamical range or over a larger respectable range that exhibited converging trends but nonetheless failed to fully plateau important diagnostics like nickel production.

Kushnir & Katz (2020) argue many of these studies suffered premature ignition from numerically unstable evolutions attributed to zone sizes (or smoothing lengths) being substantially larger than scales over which detonations develop, a common and well-known deficiency with global modeling (Niemeyer & Woosley 1997; Röpke et al. 2007; Seitenzahl et al. 2009). To put this scale disparity into perspective, hotspot sizes vary widely based on local physical conditions and compositions (Seitenzahl et al. 2009; Holcomb et al. 2013; Garg & Chang 2017), but can be less than a kilometer at conditions observed in many of our calculations. This is significantly smaller, often by orders of magnitude, than afforded resolutions. KK20 suggest the enforcement of burn limiters stabilizes solutions consistent with convergent behavior, and the lack of such limiters might explain previously discrepant results. Our own implementation of nucleosynthesis features a combination of temperature, energy deposition, and reactant limiters proven effective at stabilizing hydrodynamic interactions, and apply them to a tailored gridding strategy designed to concentrate computational resources near initiation sites.

In addition to the one-dimensional shock tube tests proposed by Katz & Zingale (2019), we carry out systematic convergence studies of WD collisions in 2D cylindrical symmetry, including effects of magnetic fields and helium shells triggering double detonations. Due to conformally strict meshing requirements, all of our calculations are restricted to head-on equal mass collisions. But we consider a couple of different stellar masses (0.6 and 1 M_{\odot}), a broad range of limiter parameters, toroidal and poloidal magnetic field configurations, several initial compositions (pure C/O, Mesa-generated models, helium shells), and importantly two decades of spatial resolution (1 - 100 km).

Section 2 begins with a brief discussion of our numerical methods, physical models (equation of state, reactive networks, initial data, etc.), and gridding strategies tuned to achieve high spatial resolution at detonation sites. Our results follow in section 3, and we conclude with a brief summary in section 4.

2. METHODS AND MODELS

All calculations are performed with the COSMOS++ code (Anninos et al. 2005, 2017; Anninos & Fragile 2020; Roth et al. 2022), which solves the equations for self-gravitating, Newtonian or general relativistic radiation magneto-hydrodynamics coupled with thermonuclear reactions and energy generation on unstructured, moving and adaptively refined (AMR and/or ALE) meshes. Our investigations of TDEs (Anninos et al. 2018, 2019, 2022) modeled binary encounters between WD stars and black holes with general relativistic hydrodynamics. Relativistic effects are not important in this work, so we solve instead the simpler Newtonian MHD equations together with Poisson’s equation for self-gravity.

Thermodynamics is treated with a Helmholtz equation of state, accounting for radiation, electron degeneracy, Coulomb corrections, relativistic effects, and electron-positron contributions. It is based on the Torch model (Timmes & Swesty 2000), accommodating arbitrary isotopic compositions, nuclear reaction networks, densities spanning $10^{-12} \leq \rho \leq 10^{15}$ gm cm⁻³, and temperatures $10^3 \leq T \leq 10^{13}$ K.

COSMOS++ supports several nuclear network options, including 7-, 19-, and 21-isotope alpha-chain models (Weaver et al. 1978; Timmes 1999; Anninos et al. 2018), fully coupled with hydrodynamics, advection of reactants, photodisintegration, electron capture, and nuclear energy coupling, along with an assortment of choices for the integration of stiff differential equations. We use the 19-isotope network throughout this work, which consists of the following nuclei: ⁴He, ¹²C, ¹⁶O, ²⁰Ne, ²⁴Mg, ²⁸Si, ³²S, ³⁶Ar, ⁴⁰Ca, ⁴⁴Ti, ⁴⁸Cr, ⁵²Fe, and ⁵⁶Ni, plus additional species (¹H, ³He, ¹⁴N, ⁵⁴Fe) to accommodate hydrogen burning, as well as photo-disintegration neutrons and protons.

The network is solved using a 4th order fully implicit method, incorporating a number of options to limit burn energy generation and deposition δe_{nuc} by either enforcing the energy condition $|\delta e_{nuc}|/e \leq F(\Delta t_{gas}, \Delta t_{cs}) = f_E [\Delta t_{gas}/c_{FL} \Delta t_{cs}]$ in each cell every cycle, by constraining temperature variations $|\delta T|/T \leq f_T$, by limiting fractional changes to molar abundances $|\delta Y_i|/Y_i \leq f_Y$, or all three in any combination. Here Δt_{gas} and Δt_{cs} are the hydrodynamic timestep and local sound crossing times respectively, c_{FL} is the Courant factor, e is the gas internal energy density, and (f_E, f_T, f_Y) are constants less than unity. These limiting options are applied across every hydrodynamic cycle, which typically evolves with a much greater timestep than the characteristic time required for the nuclear network to remain stable (without time-implicit solvers), or to deposit released energy into cells at a rate satisfying hydrodynamic stability conditions (for example a sound crossing time). Stability between hydrodynamics and nuclear energy production can be achieved by either increasing grid resolution, or evolving with a small enough timestep preventing excessive energy production. Although COSMOS++ offers an option to constrain timesteps based

on local estimates of energy production rates, it is not particularly effective in practice and leads to excessively long runtimes, especially for multi-dimensional calculations. Alternatively, burn limiters provide the necessary stability at hydrodynamic timescales while maintaining desired monotonic convergence with resolution. They operate in a manner similar to hydrodynamic timestep limiting, except the limit is applied to the network timestep which has the effect of scaling reaction rates to prevent excessive energy generation. Integration over these smaller reaction limiting timesteps is performed iteratively with a bisection algorithm that converges on the burn timestep required to satisfy energy production (or temperature variation) conditions. Our results are not especially sensitive to whether the bracket terms are included in the limiting process, generally agreeing with the simpler procedure ($F = f_E$), particularly at higher resolutions, so long as the constant coefficient f_E is adjusted accordingly.

Apart from the Newtonian (versus general relativistic) MHD treatment, the numerical methods concerning nucleosynthesis, reactant solvers, energy coupling, etc., are identical to our previous TDE studies, so we refer the reader to the publications listed above for details not provided here.

2.1. Magnetic Fields

A few of our models include either toroidal or poloidal magnetic fields scaled globally to a specified strength parameter β such that the ratio of magnetic to thermal pressures everywhere satisfies $P_B/P \leq \beta$. This scaling is applied only when initially mapping the stars to the grid, allowing the field amplitudes to amplify over time. The magnetic field inside the star (defined by a threshold pressure ratio $\delta_P \equiv P/P_{max} = 10^{-5}$ of the central peak P_{max}) is calculated from a single-component vector potential

$$A^i = \begin{cases} r_{cyl}^{\alpha_1} e^{-((r-r_c)/(\alpha_2 R_*))^2} & \text{if } \delta_P > 10^{-5} \\ 0 & \text{otherwise,} \end{cases} \quad (1)$$

where r is a spherical coordinate, r_{cyl} the cylindrical coordinate, r_c the star centers, R_* the star radii, and the parameters α_i are tuned to generate a desired field strength at the stellar surface once a strength parameter is chosen to set the maximum field amplitude in the core. We take $(\alpha_1, \alpha_2) = (0, 0.28)$ for toroidal fields, and $(4, 0.25)$ for poloidal. The non-zero poloidal field variable α_1 prevents excessively steep gradients of the magnetic pressure along the pole, and effectively describes a current loop potential with a radius equal to roughly half the star radius. The index on A^i represents an azimuthal component ($A^i \equiv A^\phi$) for poloidal fields, and a longitudinal one ($A^i \equiv A^z$) for toroidal.

2.2. 1D Reactive Shocks

The one-dimensional test problems proposed by [Katz & Zingale \(2019\)](#) are a set of planar shock tube configurations with the following initial conditions: uniform 5×10^6 g/cm³ density, 10^7 K temperature, -2×10^8 cm/s velocity, and -1.1×10^8 cm/s² acceleration, across a grid of length 1.64×10^9 cm. The left boundary (at $x = 0$) is a rigid reflecting wall. The right boundary is open with symmetric conditions allowing gas to flow perpetually onto the grid subject to gravitational acceleration. The compositions are initialized to either equal mass (50/50) carbon/oxygen, or 5/50/45 mass fractions He/C/O. Unlike the 2D models discussed in the next section, we do not use geometric zoning for these tests. Instead the entire grid is covered uniformly with evenly spaced cells since ignition is expected to trigger somewhere off the reflective boundary as accreting material powers the outward propagating shock front. In each case ignition is defined at the time and location where the gas temperature first reaches $T = 4 \times 10^9$ Kelvin.

2.3. 2D WD Collisions

To achieve a dynamical range broad enough to cover the nearly five decades in spatial scales needed to address stability and convergence uncertainties, we apply a static geometric zoning strategy similar to [Anminos et al. \(2022\)](#), but tuned to concentrate mesh cells near ignition sites and aligned (approximately) with developing shock structures near the polar and equatorial planes. This strategy increases cell dimensions along both axes by the product $\Delta z_{i+1} = (1 + \epsilon)\Delta z_i$, where the geometric constant ($\epsilon > 0$) depends on the number of zones covering the length of the axis (demonstrated here for the z -axis), and is recovered by bisection from

$$\Delta z_{\min} = \frac{\epsilon L_z}{(1 + \epsilon)^{N_z} - 1}, \quad (2)$$

given a target resolution Δz_{\min} (smallest cell width), number of zones N_z , and grid half-length L_z . A typical grid constructed in this fashion is shown in [Figure 1](#) with mesh lines converging onto the centroid of the binary system

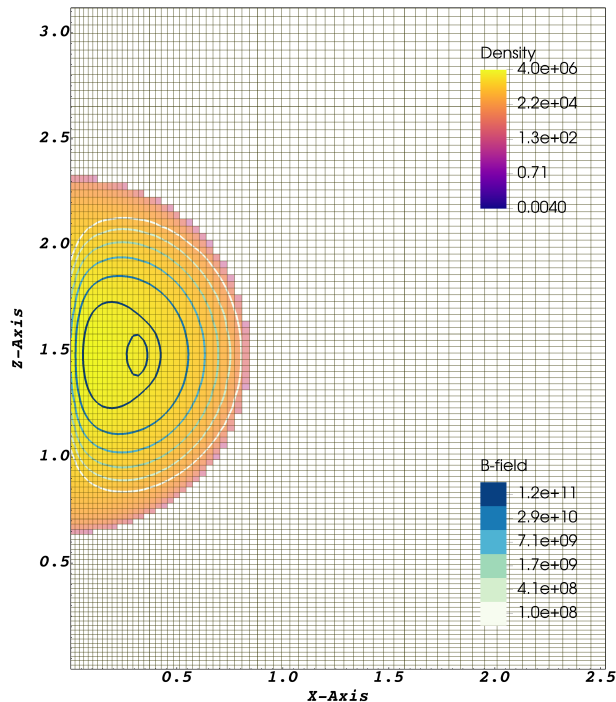


Figure 1. Sample grid demonstrating cylindrically symmetric coordinate lines geometrically converging onto both the equatorial plane where reflection boundary conditions are imposed ($z = 0$) and pole axis ($x = 0$). All collision calculations are run on similar grids but at much higher resolutions set by the maximum cell resolution and zone count along each axis. For clarification purposes, this particular image was generated at 200 km resolution. Also shown are the gas density in cgs units (with a color map) and the initial magnetic field amplitude contours in units of Gauss for the poloidal configuration. Axis labels are in units of 10^4 km.

along the trajectory-aligned axis (the z -axis), as well as the transverse direction along the equatorial plane (the x -axis projected from cylindrical coordinates). We maintain separate and distinct geometric factors to achieve desired (but independent) resolutions along each axis, with typical values $\epsilon \approx 10^{-2}$ limiting cell-to-cell size progressions to roughly 1%.

Initially the horizontal extent of the grid (along the transverse direction) is fixed at three times the maximum radius of the two stars. The vertical grid half-length L_z (along the collision trajectory) is also fixed (initially), but allowing for unequal masses, is adjusted to the separation distance between centers of mass d_0 as

$$L_z = \max \left(3R_* + d_0 \frac{M_T - M_*}{M_T} \right), \quad (3)$$

where R_* are the individual star radii, M_* are the stellar masses, M_T is the total binary mass, and the $\max()$ operation is performed over both stars in case of unequal masses. The stars are positioned either at near contact (with centers separated by a factor of 1.1 times the sum of the radii, or just beyond the L1 Lagrange point (separated by several star radii), with assigned freefall velocities

$$v_0 = \pm \frac{M_T - M_*}{M_T} v_{ff} = \pm \frac{M_T - M_*}{M_T} \sqrt{\frac{2GM_T}{d_0}}. \quad (4)$$

A summary of grid and model parameters is provided in Table 1, including masses, compositions, grid resolutions, initial separations (d_0), initial velocities (v_0), and magnetic field amplitudes in the core ($|B|_{max}$) and averaged along the surface ($|B|_{surf}$). The number of zones covering the grid varies from $N_x \times N_z = 112 \times 224$ at the coarsest (100 km) resolution to 448×896 at the finest (1 km). The greater number of zones along the z -axis allows us to maintain roughly equivalent cell resolutions when the vertical extent of the grid is increased to accommodate large initial separations.

Table 1. Collision Parameters

series	mass (M_\odot)	composition	he4 (M_\odot)	c12 (M_\odot)	o16 (M_\odot)	resolution (km)	d_0 (10^4 km)	v_0 (km/s)	$ B _{surf}$ (Gauss)	$ B _{max}$ (Gauss)
M1a	1.0	C/O	-	0.52	0.52	1-100	1.8	2100	-	-
M1b	1.0	Mesa	0.001	0.43	0.60	1-100	1.8	2100	-	-
M6a	0.6	C/O	-	0.31	0.31	1-100	1.8	2100	-	-
M6b	0.6	C/O	-	0.31	0.31	1-100	3.2	1600	-	-
M6c	0.6	C/O	-	0.31	0.31	1-100	3.2	1600	6×10^7	1×10^{11}
M6d	0.6	C/O	-	0.31	0.31	1-100	1.7	2200	1×10^8	5×10^{10}
M6e	0.6	Mesa	0.01	0.26	0.34	1-100	1.7	2200	-	-
M6f	0.6	C/O	-	0.24	0.37	1-100	1.7	2200	-	-
M6g	0.6	He/C/O	0.05	0.28	0.28	1-100	1.7	2200	-	-

This also effectively provides greater cell resolution some distance off the equatorial plane by reducing the geometric (cell-to-cell refinement) ratio.

In addition to geometric zoning, we allow the mesh to move and follow debris ejected after impact. Mesh velocity (or ALE remap) is triggered only when stellar matter is detected near the grid boundaries, and then set to

$$\dot{x}_g^i = \zeta^i \bar{v}^i \frac{x^i - x_c^i}{x_o^i - x_c^i}, \quad (5)$$

where \dot{x}_g^i is the grid velocity assigned to each cell node in vector index notation, ζ^i is a constant different along each axis but adjusted in time based on the proximity of material to grid boundaries (with typical values between 1 and 2), \bar{v}^i is the mass weighted fluid velocity, x^i is the grid coordinate, x_c^i is the mass centroid, and x_o^i is the outer grid boundary. This formulation responds to the mass-weighted Lagrangian fluid velocity while respecting geometric spacing and at the same time preventing nodes from punching through their neighbors by linearly distributing the mesh velocity outward from the centroid containing the highest mesh concentration.

Symmetric boundary conditions are imposed at all open boundaries, allowing the possibility of significant outflow at late times. In addition, a high order multipole expansion for the gravity potential adjusts to evolving tidal forces, and reflection boundary conditions across both polar and equatorial (for equal mass collisions) saves computational time. The multipole boundary conditions are centered on the mass centroid and include moments up to 10th order. Outside the stars we impose a background density of $10^{-8} \rho_{\max}$ and pressure $10^{-5} p_{\min}$, where ρ_{\max} and p_{\min} are the maximum core density and minimum pressure at the surface of both stars. Though they play no role in the evolutions, we maintain these floor values throughout the calculations. The calculations are terminated when the relative nuclear energy production (defined as the ratio of energy generated per cycle to the total accumulated energy produced) drops below 0.5%.

3. RESULTS

3.1. 1D Reactive Shocks

Figures 2 and 3 compare ignition times and locations as a function of cell resolution from the two different composition tests (pure C/O shown in red, He/C/O in black), run with three different hydrodynamics solver options: second order piecewise linear flux reconstruction (labeled ‘pwl’), third order piecewise parabolic reconstruction (labeled ‘ppm’), and filtered piecewise parabolic (‘ppm:filter’). The third ‘ppm:filter’ option uses third order flux reconstruction, but, in order to compare our results against KK20, additionally applies a grid-based filter to suppress nuclear reactions in the first zone off the reflection boundary. These options are applied across nine grid resolutions ranging from 100 to 0.2 km, and repeated for two versions of the burn limiter: one limits the energy generation and deposition to 4% of the internal fluid energy ($f_E \equiv |\delta e_{nuc}|/e = 0.04$), and the second constrains temperatures to 1% relative change cycle to cycle ($f_T \equiv |\delta T|/T = 0.01$). In both versions, limiting is enforced with an iterative bisection procedure that converges on a local timestep satisfying the imposed constraints.

Several important conclusions can be drawn from these results. First, although we have not presented calculations of the C/O test with different hydro options, we note that the displayed ppm results are identical to both the pwl and ppm+filter options. The C/O test additionally appears largely insensitive to resolutions below 20 km, where the ignition time and location curves flatten at ~ 3.8 sec and ~ 4600 km to better than a few percent, in good agreement with Figure 1 of KK20.

Next, our results for the He/C/O case are generally consistent with both KZ19 and KK20 in that we observe different behaviors depending on grid resolution. At coarse resolutions ($\gtrsim 10$ km) initiation apparently triggers at random locations. At 5 km or better (depending on hydro solver options and limiter procedures) the initiation site converges to about 1900 km from the boundary at ~ 1.4 sec, in reasonable agreement with KK20, but differing from KZ19 by about a factor of two. It is not clear why our results (and those of KK20) differ from KZ19 by such an amount, other than perhaps due to the simplified 13-isotope network used by KZ19, or to different numerical solvers. KK20 attribute the unstable behavior at coarse resolution to fast reaction rates fueling artificial hotspots seeded by numerically generated sound waves at the reflection boundary. They further demonstrate this numerical instability can be suppressed with a burn filter (mask) to prevent nuclear reactions at the reflection boundary, or by decreasing the artificially generated hotspot width by increasing resolution. Figures 2 and 3 confirm both conjectures. Comparing the dotted curve against the dot-dashed in Figure 2, we observe the filter increases stability by nearly two orders of magnitude as measured by the resolution at which the convergent plateau first develops (at 1, 5, and 50 km for the ppm, pwl, and filtered calculations respectively). Interestingly we do not observe the same benefit by masking nuclear reactions when limiting the temperature in place of energy. In that case, as shown in Figure 3, all three hydro options behave similarly at less than 10 km, and converge nicely somewhere between 2 to 5 km.

Considering the importance of burn limiters, we present in Figure 4 parameter studies demonstrating the effects of limiting either temperature or energy. The calculations were carried out at fixed 1 km resolution where results (from Figures 2 and 3) appear well-resolved, while varying both limiter parameters (f_T , f_E) from 0.005 to 0.5. Apart from a slight break in the He/C/O test at $f_T = 0.05$, Figure 4 shows little sensitivity to f_T (roughly 1% and 10% variance in the C/O and He/C/O tests respectively) across two orders of magnitude. On the other hand, the energy limiter (in Figure 4) gives consistent results at $f_E > 0.01$, but begins to adversely affect the solution at smaller values as nuclear energy is increasingly neglected each cycle. Overall it is encouraging to see the different hydro methods and limiting procedures converge at roughly 5 km, so long as we restrict limiter amplitudes to $0.01 \leq (f_T, f_E) \leq 0.05$.

3.2. Axisymmetric WD Collisions

3.2.1. Unmagnetized

Figure 5 plots the total released nuclear energy and iron-group mass as a function of grid resolution resulting from the collision of two $0.6 M_\odot$ (in black) and two $1 M_\odot$ (in red) WDs with initially uniform 50/50 C/O compositions (models M1a and M6a). Here and throughout, iron-group is defined as the sum of the heaviest elements in our network: ^{44}Ti , ^{48}Cr , ^{52}Fe , ^{54}Fe , and ^{56}Ni . Seven sets of calculations were performed for each interaction at resolutions between 100 to 1 km, and for three different burn limiter options: (1) constraining cyclic temperature variations with $f_T = 0.01$, (2) constraining energy generation and deposition with $f_E = 0.01$, and (3) limiting both temperature and reactant relative changes with $f_T = 0.01$ and $f_Y \equiv \delta Y/Y = 0.4$ respectively. Notice the nuclear energy generated is relatively insensitive to grid resolution or limiter strategies, varying by less than 40% over the entire parameter space and less than 7% at cell sizes ≤ 10 km. Iron-group mass, on the other hand, is significantly more sensitive to grid resolution, limiter options, and collision parameters (represented by the two WD masses). Although the heavier mass impact is fairly robust (displaying only a modest average downward trend of about $0.003 M_\odot/\text{km}$), results from the $0.6 M_\odot$ case vary roughly by factors of two between 10 and 50 km cell sizes, but then appear to stabilize and converge to within 10% below 5 km.

We find similar converging trends for intermediate mass elements (IMEs) in Figure 6, where we plot the total calcium-group mass in the bottom plate (including ^{28}Si , ^{32}S , ^{36}Ar , and ^{40}Ca). Although we find these elements exhibit somewhat greater sensitivity to limiter parameters (20% at 5 km, roughly double the iron-group uncertainties), they appear to be less sensitive to grid resolution, remaining robust (basically plateaued) even at resolutions as coarse as 50 km. There is, however, a slight trend towards greater intermediate mass production at coarse resolutions. This effect, together with the fact that total energy released is dominated mostly by silicon production, following the same growth pattern and accounting for more than half the total energy before nickel forms in quantity, accounts for the insensitivity of total energy released (in Figure 5) to nickel production. Even at our highest resolution, the mass

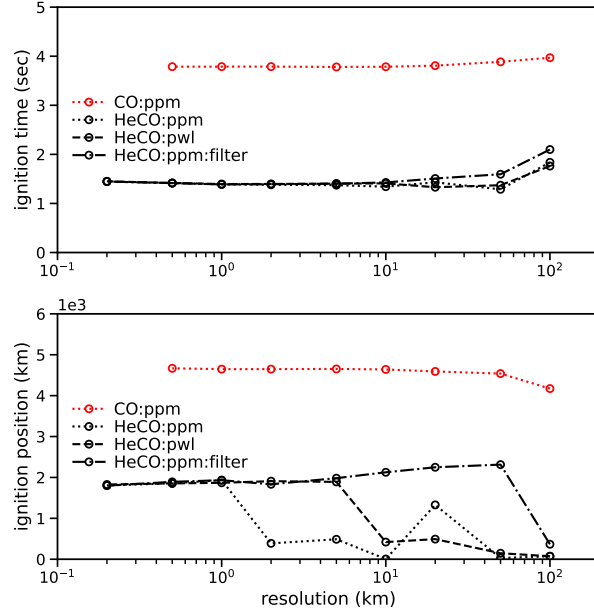


Figure 2. Time of ignition (top) and location of initiation point (bottom) from the 1D reactive shock tests plotted as a function of grid resolution with a fixed energy limiter $f_E = 0.04$. Red curves correspond to the pure C/O test, black curves to the He/C/O test with each line type representing results from the different solver options discussed in the text. Ignition is defined at the time and place where the temperature first exceeds 4×10^9 K.

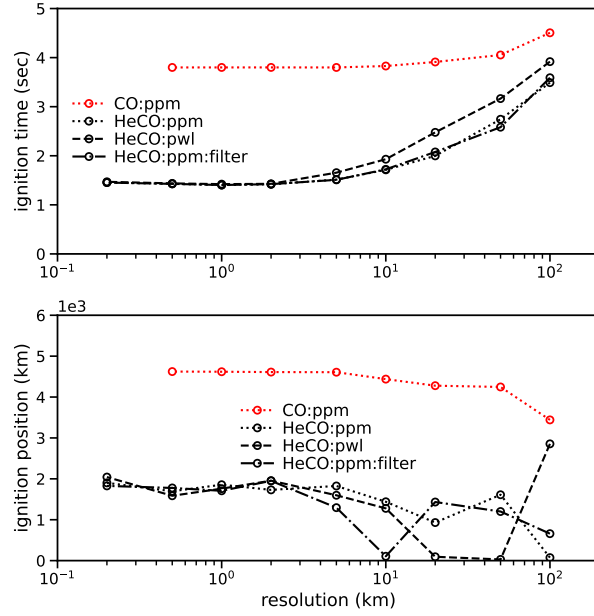


Figure 3. As Figure 2 except for a temperature limiter $f_T = 0.01$.

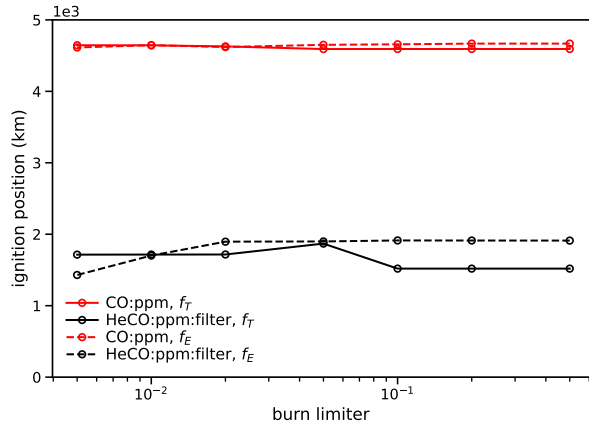


Figure 4. Ignition position is plotted as a function of the burn limiter amplitude (f_T or f_E) at fixed 1 km grid resolution. Solid (dotted) lines represent results by limiting temperature (energy).

fraction of silicon exceeds that of nickel, and any loss of energy due to the lack of iron-group production at coarse resolutions is essentially made up by making more IMEs.

Burn limiter sensitivities are demonstrated in Figure 7 for the iron-group mass plotted as a function of limiter amplitude (f_T or f_E). All calculations in the figure are performed at the same grid resolution of 5 km, determined by Figure 5 to be reasonably well converged. Although we observe the energy generated to be largely insensitive to limiter procedures or parameters, the iron-group mass on the other hand exhibits order of magnitude uncertainties when allowed fractional variations (in either temperature or energy) are relaxed to 10% or greater. We additionally point out that the energy limited iron-group mass (dotted line in the bottom plate) drops at a slightly faster rate than either of the temperature limiter curves (solid and dashed lines), suggesting values $f_E < 0.01$ are too restrictive and begin to impact the hydrodynamics in a manner similar to what is observed in Figure 4 from the 1D shocktube test.

On the whole, these results suggest that over the parameter space considered here ($0.005 \leq (f_T, f_E) \leq 0.5$), there is a lower bound on f_E below which energy release is visibly affected, and an upper bound on f_T where the two limiting procedures begin to stray from each other resulting in unreliable behavior. Values around 0.01-0.03 represent a reasonable compromise between reliability and consistency for both energy and temperature limiters, and result in well behaved monotonically converging solutions with just 10% uncertainty at 5 km resolution. Table 2 summarizes our results by tabulating the total nuclear energy released (e_{nuc}), iron-group mass (M_{Fe}), and calcium-group mass (M_{Ca}) using different limiter parameters at 1 km and 5 km resolutions.

3.2.2. Magnetized

In this section we study the convergence of nuclear reactions from colliding $0.6 M_\odot$ magnetized white dwarf stars. We consider both toroidal (series M6c) and poloidal (series M6d) configurations with parameters tabulated in Table 1. Field amplitudes are normalized by enforcing $\beta = 0.03$ in the core and choosing α_i in equations (1) which produce fields in the central core that are within theoretical bounds, and surface amplitudes that sample the high end of observations (Franzon & Schramm 2015; Putney 1995; Schmidt & Smith 1995). For this purpose we define surface amplitude to mean the field strength at a radial distance of $0.9 R_*$.

Figure 8 shows two images from the toroidal field case (M6c) at 2 km resolution taken at two different times: 6.6 secs from the start of the simulation (left), and 7.4 (right). The left plate corresponds to a time immediately after impact when the collisional shock is well established at about 2×10^3 km in the vertical direction as it begins to propagate through the star. Nearly a second later in the right image the burn front has traversed the entire star, reaching the opposite surface along the pole as the heavy elements formed in its wake are ejected along the x -axis. Each plate is composed of four quadrants imaging the temperature (top left), nickel density (top right), carbon density (bottom left, providing a measure of unburnt gas), and calcium density (bottom right), all in cgs units. Also plotted in each quadrant are contour levels of the magnetic field amplitude in Gauss units. Notice the field contours track the shock structure as it evolves, but the magnetic pressure does not amplify significantly enough to disrupt reactive flows nor affect burn product distributions in any significant way.

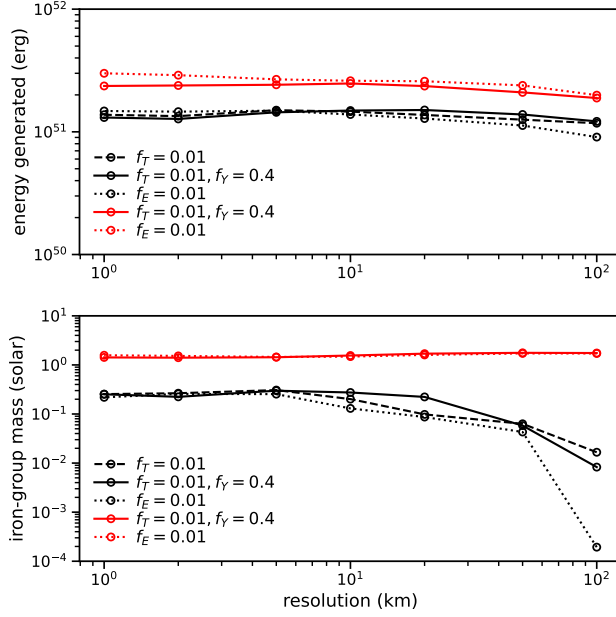


Figure 5. Total nuclear energy generated (top) and final iron-group mass (bottom) as a function of grid resolution. Black (red) represents results from the collision of two 0.6 (1.0) M_{\odot} stars. The various line types correspond to different implementations of limiters as indicated in the figure legend and discussed in the text. The iron-group mass sums densities from the production of ^{44}Ti , ^{48}Cr , ^{52}Fe , ^{54}Fe , and ^{56}Ni .

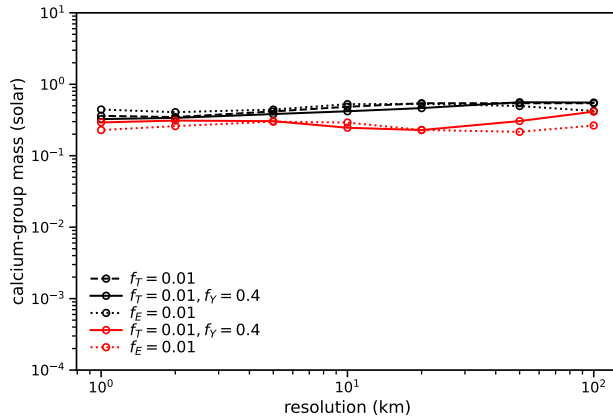


Figure 6. Total calcium-group mass (including ^{28}Si , ^{32}S , ^{36}Ar , and ^{40}Ca) is plotted as a function of grid resolution. Black (red) curves represent results from the collision of two 0.6 (1.0) M_{\odot} stars.

We additionally evaluate how or if tidal forces developing from greater initial separations affect the near-contact results from the previous section by placing the mass centers in models M6b and M6c just outside the L1 Lagrange point (corresponding to nearly four star radii). The results are presented in Figure 9 showing the energy released and iron-group masses from four calculations: unmagnetized at contact (M6a, solid black line), unmagnetized at L1 separation (M6b, solid red line), magnetized with a poloidal field at contact (M6d, dashed black line), and magnetized with a toroidal field at L1 (M6c, dashed red line). Results from the highest resolution runs are tabulated in Table 2, demonstrating excellent agreement with the models in the previous section despite differences in separations and the inclusion or configuration of magnetic fields.

3.2.3. Ignition Sites

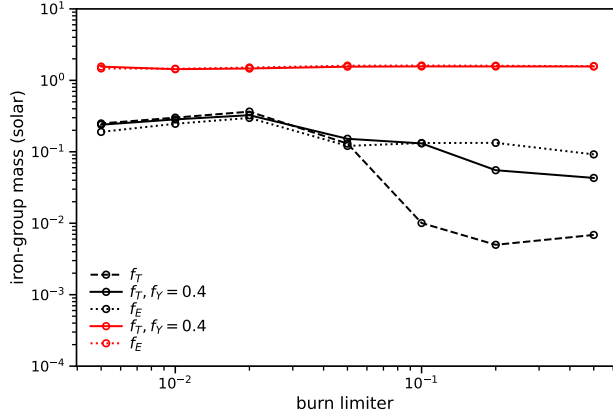


Figure 7. Total iron-group mass from the collision of two $0.6 M_{\odot}$ (black) and $1 M_{\odot}$ (red) WDs is plotted as a function of burn limiter amplitude (f_T or f_E). All calculations were run at 5 km resolution.

Table 2. Collision Results

Series	f_E	f_T	f_Y	Resolution (km)	e_{nuc} (10^{51} ergs)	M_{Fe} (M_{\odot})	M_{Ca} (M_{\odot})
M1a	0.01	-	-	1(5)	3.0(2.7)	1.57(1.45)	0.42(0.55)
"	-	0.01	0.4	1(5)	2.4(2.4)	1.42(1.43)	0.54(0.55)
M1b	-	0.04	-	1(5)	1.8(1.7)	1.42(1.52)	0.30(0.27)
M6a	0.01	-	-	1(5)	1.5(1.5)	0.22(0.25)	0.75(0.78)
"	-	0.01	-	1(5)	1.4(1.5)	0.25(0.31)	0.59(0.71)
"	-	0.01	0.4	1(5)	1.3(1.4)	0.25(0.30)	0.56(0.69)
M6b	0.01	-	-	1(5)	1.5(1.4)	0.24(0.20)	0.40(0.48)
M6c	0.01	-	-	1(5)	1.4(1.4)	0.23(0.20)	0.39(0.47)
M6d	0.01	-	-	1(5)	1.4(1.4)	0.29(0.23)	0.33(0.42)
M6e	-	0.04	-	1(5)	0.9(0.9)	0.03(0.03)	0.44(0.57)
M6f	-	0.04	-	1(5)	0.9(0.8)	0.04(0.02)	0.55(0.54)
M6g	-	0.04	-	1(5)	0.8(0.9)	0.04(0.05)	0.42(0.56)

The relative smoothness of the convergence plots can mask important differences in the development, orientation, timing, and number of ignition sites. For example, our calculations find two distinctly different evolutionary tracks distinguishing low (> 5 km) from high (< 5 km) grid resolution. All calculations appear to develop multiple shock-triggered ignition sites: a primary site at the origin or initial point of contact, and delayed secondary sites further out in radius. However, as demonstrated in Figure 10, the location of these secondary sites depends on resolution, forming a few thousand kilometers from the primary ignition site either along the pole axis at coarse resolution, or along the reflection plane at high resolution.

Both plates of Figure 10 image the density of silicon from the M6d series as a diagnostic of early ignition, along with contours of the total gas density demonstrating the compression state of the star. The top plate corresponds to 20 km resolution, the bottom to 2 km. These images are plotted on the same spatial scale, zoomed into the interior of the star to identify the shock structure, but are taken at two different times separated by approximately 0.5 seconds (2.9 secs in the top plate, 2.4 secs in the bottom). Both images exhibit a common initiation site at the origin, and secondary sites offset from the origin along orthogonal axes. In both cases, the secondary sites are triggered by shock compression and heating: the coarse resolution case is triggered by the upward moving shock generated at the point of contact, and the fine resolution case is triggered by the transverse moving shock while compressing and ejecting

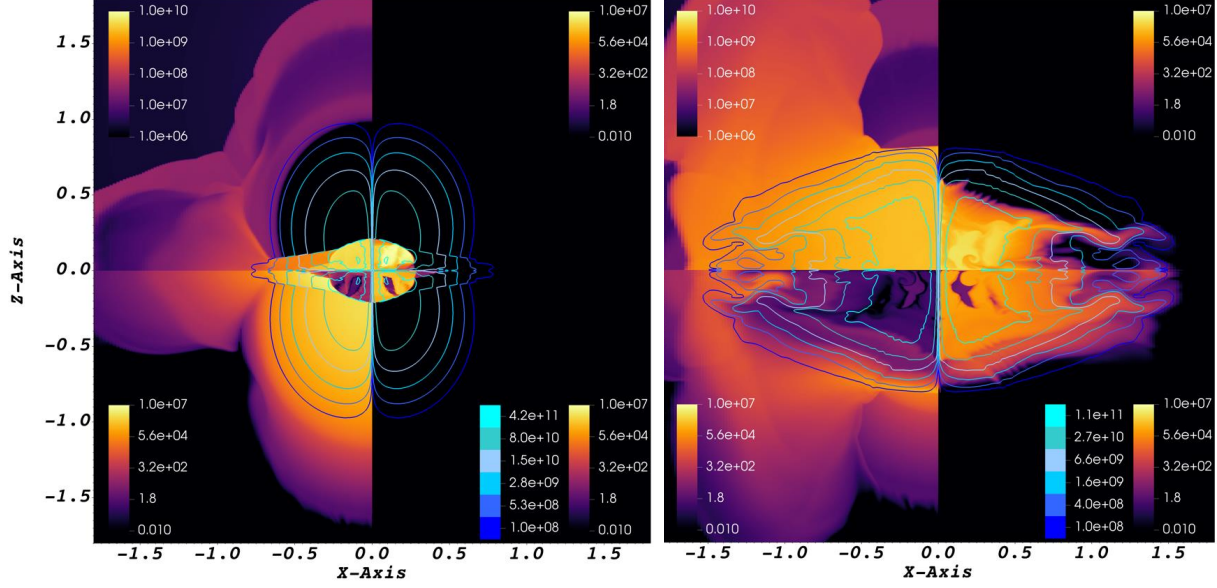


Figure 8. Evolution sequence from the magnetized collision of two $0.6 M_{\odot}$ stars, showing in each of the plates the temperature (top left), carbon density (bottom left), nickel density (top right), and calcium density (bottom right). Our calculations impose reflection (and polar) boundary conditions along the equatorial plane (and pole axis) - we do not simulate the entire domain, as perhaps these plates might suggest, but merely stack images of the different fields into different quadrants for visualization purposes. Also shown are line contours of the (toroidal) magnetic field amplitude in Gauss units. The left plate corresponds to an early time (6.6 s) immediately following the impact, shock formation, and detonation as the burn front begins to move radially outward from the initiation site; the right plate to a later time (7.4 s) when the burn front reaches the opposite surface along the pole and heavy elements eject along the collision plane (right). Axes labels are in units of 10^4 km.

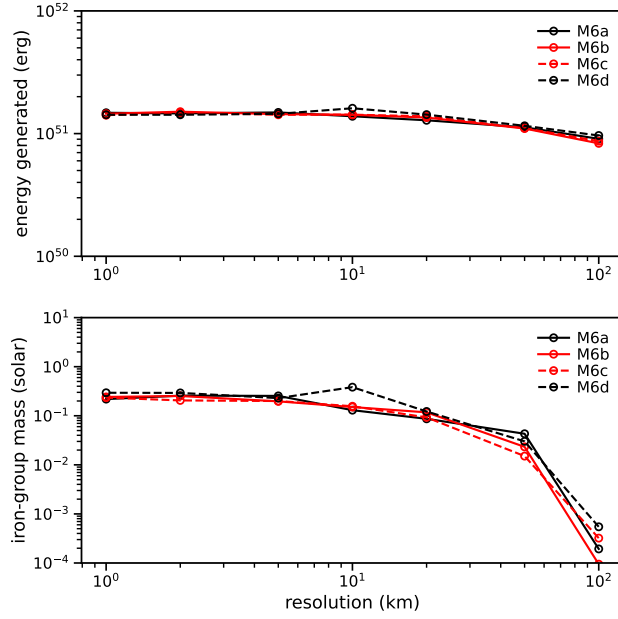


Figure 9. As Figure 5 except here we compare collisions of $0.6 M_{\odot}$ magnetized and unmagnetized stars, and from different initial separations. Black (red) lines correspond to contact (L1 Lagrange point) separations, and solid (dashed) lines represent unmagnetized (magnetized) configurations.

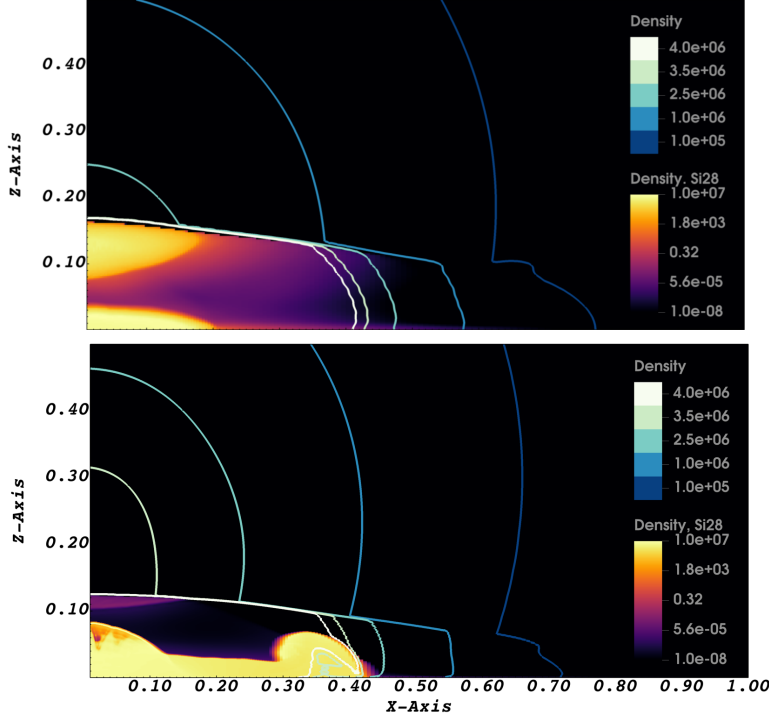


Figure 10. The effect of grid resolution on the development, orientation, and timing of multiple, nearly simultaneous, ignition sites is demonstrated by imaging the silicon density from two calculations differing only by resolution: 20 km (top, shown at 2.9 seconds) and 2 km (bottom, at 2.4 seconds). This particular image corresponds to the poloidal magnetized model M6d, but is typical of unmagnetized models as well. The five contours represent total density in cgs units, including all elements. As usual, axes labels are in units of 10^4 km.

material outward along the equatorial plane. The total gas density contours indicate the approximate location of the enveloping (multi-dimensional) shock structure. At coarse resolution, compression heating along the transverse direction (x -axis) is not adequately captured so the star does not develop secondary hot spots until later in time when the upward moving shock and the gravitationally collapsing star conspire to produce shock heated densities and temperatures high enough to initiate silicon burn along the pole.

The delay in ignition time (roughly 0.5 seconds) due to grid resolution is shown in Figure 11 where we plot the time evolution of the total masses of oxygen, silicon, calcium, and nickel for the two runs at 20 km resolution (dotted lines) and 2 km (solid lines). Despite these starkly different evolutionary tracks (in both timing and the development of hot spots), the end results, quantified by the total nuclear energy released and production yields, appear not to be especially sensitive to these differences. We attribute this to the relative proximity of the multiple nucleating sites to each other and to the point of contact, allowing the different detonation sources to quickly fuse into a single, outwardly propagating burn front. There are sufficient C/O fuel reserves pre-conditioned by gravitational free-fall to sustain thermonuclear burn throughout the entire star once ignition is achieved, regardless of the initiation sequence.

3.2.4. Mesa Compositions and Helium Shells

Because of the high uncertainty exhibited by the 1D reactive He/C/O shocktube tests in section 3.1, we explore here the effect of introducing helium to our initial WD model compositions. We consider two compositions: the first model M6e is derived directly from the Mesa stellar evolution code (Paxton et al. 2011), mapped onto the grid as described in Anninos et al. (2019), and plotted in Figure 12 for a $0.6 M_{\odot}$ WD; the second M6g utilizes a 50/50 mixture of C/O in the interior of the star but replaces all elements in the outer 2000 km shell with pure helium. We anticipate (and observe) model M6g to undergo double detonation ignition, burning simultaneously radially outward from the C/O core as well as spherically through the helium shell (Townsend et al. 2019; Boos et al. 2021). Both models were calculated without and with the artificial filter near the equatorial plane (which added stability to the 1D shocktube

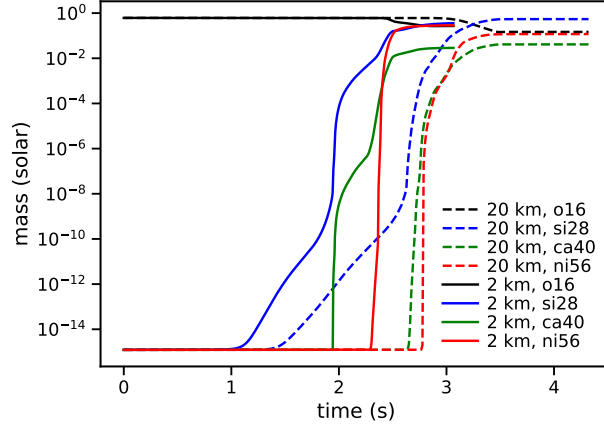


Figure 11. Total mass of a few select elements from model M6d (oxygen in black, silicon in blue, calcium in green, and nickel in red) as a function of time. Solid and dashed lines represent results from the 2 and 20 km resolution calculations from Figure 10, correlating ignition time to grid resolution.

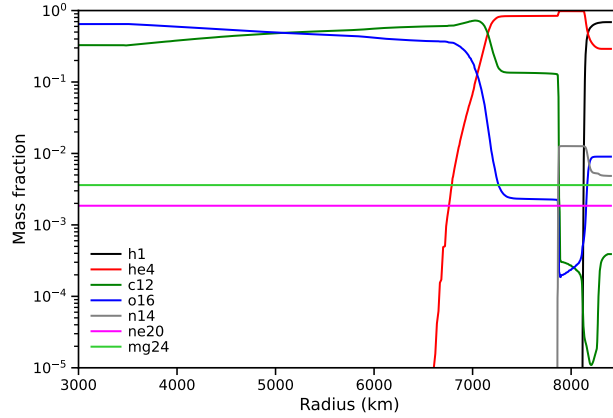


Figure 12. Dominant composition profiles derived from the Mesa stellar evolution code for a 0.6 solar mass WD as a function of radius.

tests). Interestingly we find the filter has no significant effect on convergence or final production outcomes. What was unpredictable or random in the shock tube test was the location and timing of the initiating hotspot. However, and as we pointed out in the previous section, once detonation triggers in these models it matters little how far off the equatorial plane it first ignited.

Figure 13 shows a couple of time instances from the double detonation model M6g. Two prominent burn fronts ignite nearly simultaneously and propagate separately through the helium shell along the outer surface of the star and radially outward from the center of the C/O core. This figure plots the silicon density corresponding to the 2 km resolution case, but we note that the 1 km case behaves identically: The two wave fronts burn robustly enough to reach the opposite ends of the star at about the same time. However, the robustness and sustainability of the detonation front across the outer shell depends strongly on grid resolution. For example, at intermediate resolutions (5 to 10 km) the surface wave front propagates slower than in the high resolution (1 to 2 km) cases, and is swept up by the stronger (core) detonation very early. At even coarser resolutions (≥ 20 km), hotspots are created in the helium shell near the collision plane, but the burning cannot sustain itself and the front essentially freezes in place (does not propagate) until the core detonation overtakes it. Additionally we find that even for the highest resolution models, the helium shell does not produce significant amounts of iron group products but is nevertheless a strong source of intermediate mass elements, from silicon to calcium.

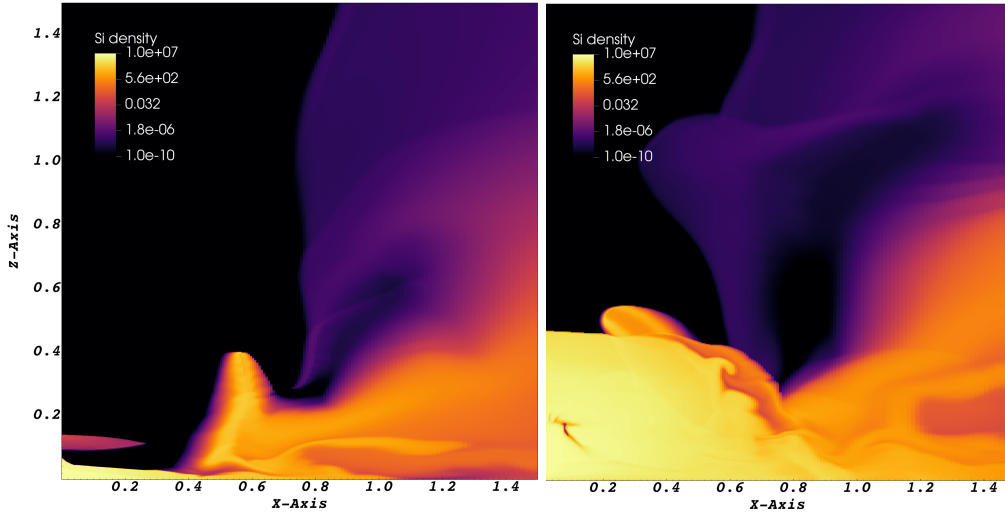


Figure 13. Silicon density from model M6g imaged at two different times: 2.6 seconds (left) and 3.4 (right). The early image shows clear evidence of multiple and nearly simultaneous initiation sites, including the stellar center, the vertical offset immediately behind the upward moving hydrodynamic shock, and the detonation running through the outer helium shell. The late image shows the helium shell front reaching the opposite axis at about the same time as the main (stronger) detonation traveling radially outward from the star center.

Figure 14 plots the total nuclear energy released (top) and iron-group production (bottom) comparing models M1b, M6e, M6f, and M6g as a function of grid resolution. We find convergence patterns similar to the pure C/O models, except at relatively diminished values with fewer burn products and less released energy. However, differences in the conversion efficiency are attributed to different C/O mixtures not to helium content as observed by comparing the excellent agreement between models M6e and M6f, a pure C/O WD composed of roughly the same 40/60 mixture as M6e. This behavior is typical of carbon-depleted cores as they generally require higher imploding shock strengths to sustain detonations (Seitenzahl et al. (2009) for example finds larger critical hotspot radii in reduced carbon mixtures).

4. CONCLUSIONS

We have explored the stability, reliability, and general convergence behavior of nuclear reactive flow calculations from the head-on collision of two equal mass white dwarf stars. Our motivation is derived from calculations in the literature that have not always agreed quantitatively on important diagnostics like the amount of iron-group products produced in these scenarios. We are also somewhat skeptical about claims of convergence, and the always-worrisome possibility that the application of limiters might have unintended consequences, particularly if they are applied arbitrarily and without careful study.

For this work we considered equal mass collisions of $0.6 M_{\odot}$ and $1 M_{\odot}$ stars, simulated on geometrically refined grids specially designed to concentrate resources at initiation sites along the equatorial and polar planes. Calculations were carried out at resolutions ranging from 100 to 1 km, and stabilized with several reaction limiting procedures, including by energy released, temperature variations, and local reactant changes. We find generally consistent results independent of limiter procedures (or what field is limited) when limiter amplitudes are bounded on both the low and high ends. For example, at $f_E < 0.01$ the hydrodynamic solutions maintain their convergent properties but the

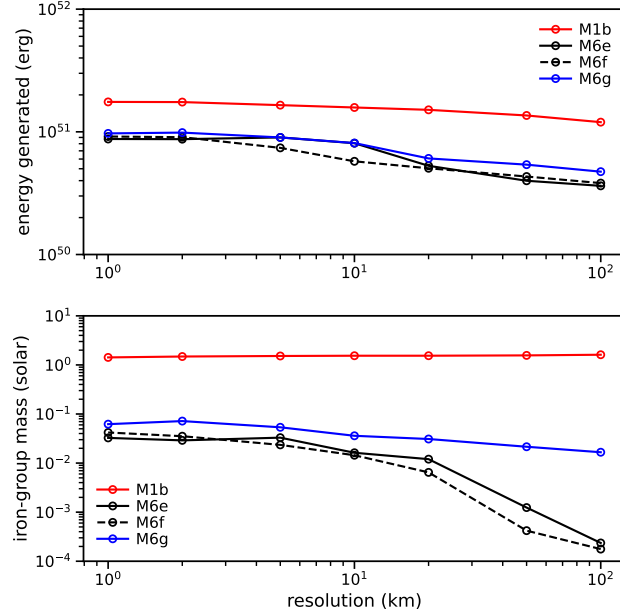


Figure 14. As Figures 5 and 9 except for the He/C/O composition cases M1b (Mesa composition), M6e (Mesa composition), M6f (40/60 C/O), and M6g (50/50 C/O with He shell).

strong limiting of energy creation begins to affect the thermodynamic behavior, resulting in solutions deviating more and more from the temperature-limited solutions. Additionally, although energy limiting tolerates large amplitudes, limiting by temperature does not, so that values of $f_T > 0.05$ tend to produce unstable or at best unreliable solutions.

Across the restricted range $0.01 < (f_T, f_E) < 0.05$, we found all versions of limiting procedures produced consistently stable solutions, with well-behaved, monotonic trends towards convergence with uncertainties better than 10% at 5 km resolution (when compared to the 1 km results) for total energy released and iron-group mass, and about 20% for intermediate (calcium-group) elements. Increasing resolution stabilizes the number, location, and development of initiation sites, as well as securing the sustainability of detonation waves through helium surface shells. These results hold for both unmagnetized and magnetized models, for simple C/O or more complex Mesa core compositions, with or without outer helium shells, and regardless of whether the two stars are initialized at contact or separated by multiple stellar radii.

Similar conclusions are drawn from our 1D reactive shock tests. There we also found evidence of clear convergence at a few kilometers resolution, and inferred comparable (lower and upper bound) restraints on limiter amplitudes. We point out that these results are generally consistent with earlier work on axisymmetric collisions of WDs (Kushnir et al. 2013), and with tidal disruptions of stars by black holes (Anninos et al. 2022). The latter applied a similar analysis approach to a very different binary interaction, but arrived at essentially the same conclusions.

ACKNOWLEDGMENTS

This work was performed under the auspices of the U.S. Department of Energy by Lawrence Livermore National Laboratory under Contract DE-AC52-07NA27344.

Software: Cosmos++ (Anninos et al. 2005, 2017; Anninos & Fragile 2020; Roth et al. 2022), Torch (Timmes 1999)

REFERENCES

- Anninos, P., Bryant, C., Fragile, P. C., et al. 2017, ApJS, 231, 17, doi: [10.3847/1538-4365/aa7ff5](https://doi.org/10.3847/1538-4365/aa7ff5)
- Anninos, P., Camarda, K. D., Estes-Myers, B., & Roth, N. 2022, ApJ, 934, 157, doi: [10.3847/1538-4357/ac7b87](https://doi.org/10.3847/1538-4357/ac7b87)

- Anninos, P., & Fragile, P. C. 2020, *ApJ*, 900, 71,
doi: [10.3847/1538-4357/abab9c](https://doi.org/10.3847/1538-4357/abab9c)
- Anninos, P., Fragile, P. C., Olivier, S. S., et al. 2018, *ApJ*, 865, 3, doi: [10.3847/1538-4357/aadad9](https://doi.org/10.3847/1538-4357/aadad9)
- Anninos, P., Fragile, P. C., & Salmonson, J. D. 2005, *ApJ*, 635, 723, doi: [10.1086/497294](https://doi.org/10.1086/497294)
- Anninos, P., Hoffman, R. D., Grewal, M., Lavell, M. J., & Fragile, P. C. 2019, *ApJ*, 885, 136,
doi: [10.3847/1538-4357/ab4ae0](https://doi.org/10.3847/1538-4357/ab4ae0)
- Boos, S. J., Townsley, D. M., Shen, K. J., Caldwell, S., & Miles, B. J. 2021, *ApJ*, 919, 126,
doi: [10.3847/1538-4357/ac07a2](https://doi.org/10.3847/1538-4357/ac07a2)
- Franzon, B., & Schramm, S. 2015, *PhRvD*, 92, 083006,
doi: [10.1103/PhysRevD.92.083006](https://doi.org/10.1103/PhysRevD.92.083006)
- García-Senz, D., Cabezón, R. M., Arcones, A., Relaño, A., & Thielemann, F. K. 2013, *MNRAS*, 436, 3413,
doi: [10.1093/mnras/stt1821](https://doi.org/10.1093/mnras/stt1821)
- Garg, U., & Chang, P. 2017, *ApJ*, 836, 189,
doi: [10.3847/1538-4357/aa5d58](https://doi.org/10.3847/1538-4357/aa5d58)
- Hawley, W. P., Athanassiadou, T., & Timmes, F. X. 2012, *ApJ*, 759, 39, doi: [10.1088/0004-637X/759/1/39](https://doi.org/10.1088/0004-637X/759/1/39)
- Holcomb, C., Guillochon, J., De Colle, F., & Ramirez-Ruiz, E. 2013, *ApJ*, 771, 14, doi: [10.1088/0004-637X/771/1/14](https://doi.org/10.1088/0004-637X/771/1/14)
- Katz, M. P., & Zingale, M. 2019, *ApJ*, 874, 169,
doi: [10.3847/1538-4357/ab0c00](https://doi.org/10.3847/1538-4357/ab0c00)
- Kushnir, D., & Katz, B. 2020, *MNRAS*, 491, 3760,
doi: [10.1093/mnras/stz3285](https://doi.org/10.1093/mnras/stz3285)
- Kushnir, D., Katz, B., Dong, S., Livne, E., & Fernández, R. 2013, *ApJL*, 778, L37, doi: [10.1088/2041-8205/778/2/L37](https://doi.org/10.1088/2041-8205/778/2/L37)
- Lorén-Aguilar, P., Isern, J., & García-Berro, E. 2010, *MNRAS*, 406, 2749,
doi: [10.1111/j.1365-2966.2010.16878.x](https://doi.org/10.1111/j.1365-2966.2010.16878.x)
- Niemeyer, J. C., & Woosley, S. E. 1997, *ApJ*, 475, 740,
doi: [10.1086/303544](https://doi.org/10.1086/303544)
- Papish, O., & Perets, H. B. 2016, *ApJ*, 822, 19,
doi: [10.3847/0004-637X/822/1/19](https://doi.org/10.3847/0004-637X/822/1/19)
- Paxton, B., Bildsten, L., Dotter, A., et al. 2011, *ApJS*, 192, 3, doi: [10.1088/0067-0049/192/1/3](https://doi.org/10.1088/0067-0049/192/1/3)
- Putney, A. 1995, *ApJL*, 451, L67, doi: [10.1086/309689](https://doi.org/10.1086/309689)
- Raskin, C., Scannapieco, E., Rockefeller, G., et al. 2010, *ApJ*, 724, 111, doi: [10.1088/0004-637X/724/1/111](https://doi.org/10.1088/0004-637X/724/1/111)
- Röpke, F. K., Woosley, S. E., & Hillebrandt, W. 2007, *ApJ*, 660, 1344, doi: [10.1086/512769](https://doi.org/10.1086/512769)
- Rosswog, S., Kasen, D., Guillochon, J., & Ramirez-Ruiz, E. 2009, *ApJL*, 705, L128,
doi: [10.1088/0004-637X/705/2/L128](https://doi.org/10.1088/0004-637X/705/2/L128)
- Roth, N., Anninos, P., Robinson, P. B., et al. 2022, *ApJ*, 933, 226, doi: [10.3847/1538-4357/ac75cb](https://doi.org/10.3847/1538-4357/ac75cb)
- Schmidt, G. D., & Smith, P. S. 1995, *ApJ*, 448, 305,
doi: [10.1086/175962](https://doi.org/10.1086/175962)
- Seitenzahl, I. R., Meakin, C. A., Townsley, D. M., Lamb, D. Q., & Truran, J. W. 2009, *ApJ*, 696, 515,
doi: [10.1088/0004-637X/696/1/515](https://doi.org/10.1088/0004-637X/696/1/515)
- Timmes, F. X. 1999, *ApJS*, 124, 241, doi: [10.1086/313257](https://doi.org/10.1086/313257)
- Timmes, F. X., & Swesty, F. D. 2000, *ApJS*, 126, 501
- Townsley, D. M., Miles, B. J., Shen, K. J., & Kasen, D. 2019, *ApJL*, 878, L38, doi: [10.3847/2041-8213/ab27cd](https://doi.org/10.3847/2041-8213/ab27cd)
- Weaver, T. A., Zimmerman, G. B., & Woosley, S. E. 1978, *ApJ*, 225, 1021, doi: [10.1086/156569](https://doi.org/10.1086/156569)